UCLA
UCLA Previously Published Works

Title

Conducting thermal energy to the membrane/water interface for the enhanced desalination of hypersaline brines using membrane distillation

Permalink

https://escholarship.org/uc/item/6mt5p27w

Authors

Wang, Jingbo
Liu, Yiming
Rao, Unnati
et al.

Publication Date

2021-05-01

DOI

10.1016/j.memsci.2021.119188

Peer reviewed

eScholarship.org Powered by the California Digital Library
University of California

Journal of Membrane Science 626 (2021) 119188

Contents lists available at ScienceDirect

Journal of Membrane Science

journal homepage: http://www.elsevier.com/locate/memsci

Conducting thermal energy to the membrane/water interface for the enhanced desalination of hypersaline brines using membrane distillation

Jingbo Wang [a,1], Yiming Liu [a,1], Unnati Rao [a], Mark Dudley [b], Navid Dehdari Ebrahimi [c], Jincheng Lou [b], Fei Han [d], Eric M.V. Hoek [a], Nils Tilton [b], Tzahi Y. Cath [e], Craig S. Turchi [f], Michael B. Heeley [g], Y. Sungtaek Ju [c], David Jassby [a,*]

[a] University of California Los Angeles (UCLA), Department of Civil & Environmental Engineering, California NanoSystems Institute and Institute of the Environment & Sustainability, Los Angeles, CA, USA
[b] Colorado School of Mines, Department of Mechanical Engineering, Golden, CO, USA
[c] UCLA, Department of Mechanical and Aerospace Engineering, Los Angeles, CA, USA
[d] Hebei University of Technology, School of Civil and Transportation Engineering, Tianjin, China
[e] Colorado School of Mines, Department of Civil and Environmental Engineering, Golden, CO, USA
[f] Buildings & Thermal Science Center, National Renewable Energy Laboratory, Golden, CO, USA
[g] Colorado School of Mines, Division of Economics and Business, Golden, CO, USA

ARTICLE INFO

Keywords:
Membrane distillation
Thermal desalination
Hypersaline water treatment
Gained output ratio
Specific energy consumption

ABSTRACT

Membrane distillation (MD) is a membrane-based thermal desalination process capable of treating hypersaline brines. Standard MD systems rely on preheating the feed to drive the desalination process. However, relying on the feed to carry thermal energy is limited by a decline of the thermal driving force as the water moves across the membrane, and temperature polarization. In contrast, supplying heat directly into the feed channel, either through the membrane or other channel surfaces, has the potential of minimizing temperature polarization, increasing single-pass water recoveries, and decreasing the number of heat exchangers in the system. When solar thermal energy can be utilized, particularly if the solar heat is optimally delivered to enhance water evaporation and process performance, MD processes can potentially be improved in terms of energy efficiency, environmental sustainability, or operating costs. Here we describe an MD process using layered composite membranes that include a high-thermal-conductivity layer for supplying heat directly to the membrane-water interface and the flow channel. The MD system showed stable performance with water flux up to 9 L/m^2/hr, and salt rejection >99.9% over hours of desalinating hypersaline feed (100 g/L NaCl). In addition to bench-scale system, we developed a computational fluid dynamics model that successfully described the transport phenomena in the system.

1. Introduction

Membrane distillation (MD) is a membrane-based thermal desalination process that involves the evaporation of water through a microporous, hydrophobic membrane. Common MD membrane materials include polyvinylidene fluoride (PVDF), polytetrafluoroethylene (PTFE), and polypropylene (PP) [1]. In comparison to other membrane and thermal desalination processes, MD has several advantages when treating high salinity waters, including lower operating temperature and thermal energy demand than some conventional thermal distillation processes, lower operating pressure and electrical energy demand than conventional reverse osmosis processes, and the capability to treat water of nearly any salinity up to saturation [1–4]. Though pressure-driven desalination processes such as RO are less energy intensive than MD, they are limited to salinity below 70 g/L [5]. In contrast, the performance of MD is comparably less sensitive to feedwater salinity, making it attractive for desalinating high-salinity waste streams [3,6,7].

In a standard MD system, saline feed water is heated before contacting the membrane that separates the hot feed from the distillate. As warm feed flows over the membrane, water evaporates at the water/

* Corresponding author.
E-mail address: jassby@ucla.edu (D. Jassby).
[1] These authors contributed equally.

https://doi.org/10.1016/j.memsci.2021.119188
Received 11 October 2020; Received in revised form 12 February 2021; Accepted 14 February 2021
Available online 20 February 2021
0376-7388/© 2021 Elsevier B.V. All rights reserved.

membrane interface, diffuses through the membrane pores, and condenses in the colder distillate side [8,9]. In this design, the hot feed stream serves as the thermal energy carrier to drive the desalination process; however, the reliance on the feed to carry thermal energy has limitations, including temperature polarization and overall feed stream temperature drop, which cause the driving force for evaporation to rapidly decline along the membrane (Fig. 1). Temperature polarization is caused by heat loss through the membrane, which occurs due to heat advection by the vapor and heat conduction through the vapor-filled pores and solid polymer phase of the membrane. Temperature polarization limits the thermal efficiency of MD and connects it to feed side hydrodynamics [4]. Due to temperature polarization, the temperature at the membrane surface on the feed side ($T_{m,f}$) may be substantially lower than the bulk feed temperature ($T_{b,f}$) [4,7,10–15].

Integrating renewable energy as the heat source is important for MD to become more practical and economically viable [16–19]. Several studies have successfully operated conventional MD systems by preheating the feed using solar energy. However, this approach still suffers from temperature polarization and feed temperature drop within the MD system [20–26]. In contrast, providing thermal energy directly to the membrane-water interface (where evaporation occurs) and/or through another surface in the feed channel has the potential of minimizing temperature polarization (Fig. 1), increasing single-pass water recovery, and decreasing the number of heat exchangers in the system, thus improving the energy efficiency of the lab-scale thermal process [27,28]. Several studies [4,29–36] have demonstrated the feasibility and effectiveness of direct heating, either by solar-driven photothermal membranes [4,29–34] or resistively-heated membranes [35,36]. However, studies implementing photothermal membranes report low water fluxes (below 2 L/m^2/hr (LMH)) under standard or even concentrated solar illumination [4,29–34]. Therefore, producing reasonable desalination rates requires very large membrane surface areas to be exposed to sunlight, complicating system design and increasing capital costs.

In this study, we report on an MD process in which the full length of the feed channel is actively heated by supplying heat to thermally conducting layers that were incorporated into the system (Fig. 2). We test the performance of our novel approach by treating hypersaline feeds with a bench-scale vacuum membrane distillation (VMD) system. VMD was chosen for its minimal conductive heat losses, due to the low thermal conductivity of vacuum on the distillate side [37]. The system showed stable performance with water flux up to 9 LMH, and salt rejection >99.9% over hours of operation, with heat only provided through the thermally conducting layers. Optimum system configuration, operating conditions, and specific energy consumptions are discussed. To complement the experimental studies, a computational fluid dynamics model was developed to describe the transport phenomena and explain how operating conditions impact vapor production and temperature polarization. This VMD process can potentially provide a solution to desalinating highly concentrated brines at a lower cost.

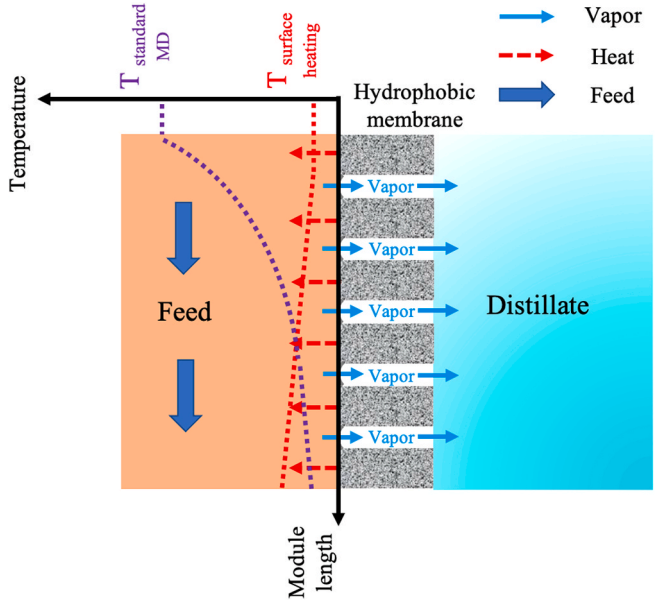

Fig. 1. Temperature profile of a standard MD and a direct heating MD system with localized heating at the feed/membrane interface.

2. Materials and methods

2.1. Materials

The polymeric membrane materials used in this study are hydrophobic PP membranes (3 M, Charlotte, NC) with a 100 μm thickness, 0.2 μm pore size, and 70% porosity. The thermally conducting layers were aluminum shims (flat aluminum sheets placed in the feed channel, not in direct contact with membrane) with a thickness of 250 μm (McMaster-Carr, Los Angeles, CA), and aluminum meshes (mesh size 120 × 120) with a thickness of 203 μm, an opening size of 109 μm, and an open area of 27%, that were in direct contact with the membrane either in the distillate channel or in the feed channel (Fig. 2). The membrane coupon, aluminum shim piece, and aluminum mesh piece were cut from flat sheets provided by the manufacturers and used directly without further modification. The synthetic hypersaline feed contained 100 g/L NaCl (~3 times seawater salinity) at room temperature. The sodium chloride was ACS grade with 99% or greater purity (Fisher Scientific, Pittsburgh, PA) and was used as received.

2.2. Direct heating VMD experiments

The experiments were performed using a fully instrumented and automated laboratory-scale cross-flow VMD system with an acetal membrane flow cell (Fig. 2a). The membrane cell housed a flat sheet membrane with an effective area of 40 cm^2 (4 cm × 10 cm). The height of the feed and distillate flow channels were 4 mm. No spacers were used in the feed channel. A piece of aluminum (Al) mesh and/or a piece of Al shim were used as the thermal conducting layer, both with a size of 15 cm × 12 cm, with the shim placed in the feed channel (not in contact with the membrane) and the mesh placed in contact with the membrane either in the feed channel or in the distillate channel (Fig. 2). These Al thermal conductors were connected to a heat source and used to deliver heat into the flow channel (more on this below). A peristaltic pump (Cole Parmer, Pump Drive Model 7553–70, Pump Head Model 77200–50, Vernon Hills, IL) with temperature resistant tubing circulated the feed solution, with the flow rates (0.4–1.6 L/min) controlled by the pump controller. A vacuum pump (JB Industries, Model Number DV-85 N, Aurora, IL) generated a vacuum in the range of 0.90–0.99 bar (vacuum gauge reading) on the distillate side of the membrane. The absolute pressure on the distillate side was determined by subtracting the pressure from the vacuum pump gauge from the atmospheric pressure (for example, 0.99 bar vacuum pump gauge reading corresponds to an absolute pressure of 1–0.99 = 0.01 bar).

The acetal membrane flow cell houses a flat sheet membrane, and thermal conducting layers that are coupled with thermal power.

Temperature sensors (Vktech, Model Number DS18b20, Shenzhen, China) monitored the feed temperature at the feed channel entrance and outlet. Salt concentrations in the distillate (C_p, M) and feed (C_F, M) were measured using a conductivity meter (Thermo Fisher Scientific, Orion Star A322, Waltham, MA), and used to calculate observed salt rejection, R, using Eq. (2):

$$R = 1 - \frac{C_p}{C_F} \tag{2}$$

The distillate flux was determined by measuring the mass change of

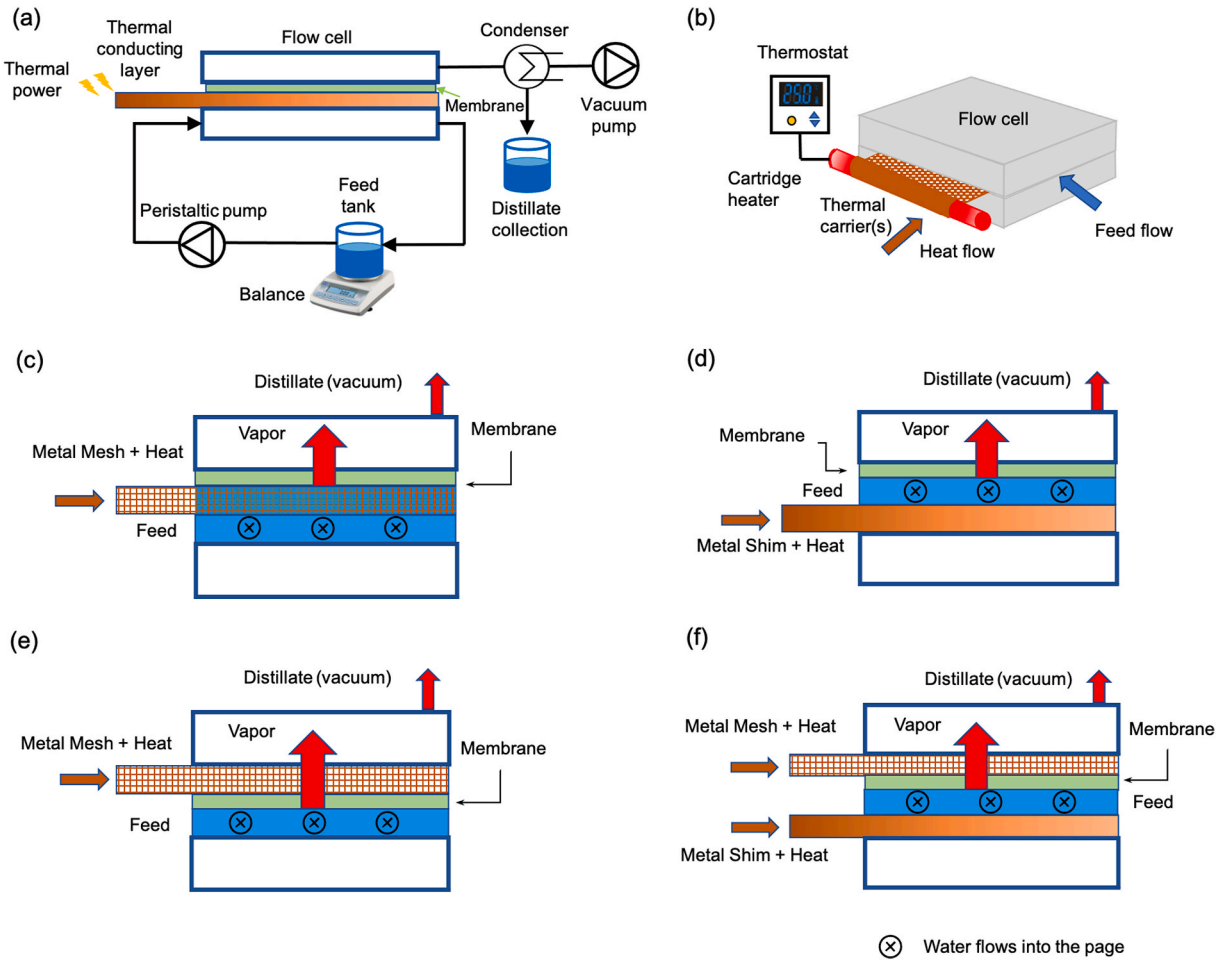

Fig. 2. (a) Schematic of a fully instrumented and automated laboratory-scale direct heating MD system operating in vacuum-assisted mode. The acetal membrane flow cell houses a flat sheet membrane, and thermal conducting layers that are coupled with thermal power. (b) Schematic of direct heating MD cell and heat source coupling system. Thermal carrier(s) were wrapped around a cartridge heater to mimic the coupling with solar power. The thermostat was used to control heat input to the system. (c) – (f) demonstrate the schematic of the direct heating MD cell configurations: (c) mesh is placed in the feed stream as the only thermal carrier, (d) shim is placed in the feed stream as the only thermal carrier, (e) mesh is on top of membrane in the distillate stream as the only thermal carrier, and (f) both shim and mesh are used as thermal carriers with shim being placed in the feed stream and mesh being placed in distillate stream. Water vapor forms at the water/membrane interface. The heat flow and feed flow directions are perpendicular.

the feed tank in real time using a scale (Ohaus, Model Number PX2202, Parsippany, NJ) set to automatically log mass data every 5 s. The feed tank was insulated with foam to minimize heat losses.

Heat was delivered to the membrane/water interface and/or the flow channel by heat conduction through the metallic thermal carriers (Al shim and mesh). Al shim and mesh were chosen to serve as the thermal conducting layer because of their good thermal conductivity, excellent mechanical strength, and low cost. When the aluminum mesh was installed in the system, the mesh was always placed in close contact with the membrane (either in the feed or the distillate) to provide surface heating. When placing the mesh on the distillate side, the mesh can be kept corrosion free and the heat is not anticipated to be lost to the environment because of the low thermal conductivity of a vacuum. Instead, the heat is expected to conduct across the membrane to the membrane/water interface. The shim was placed close to, but not in direct contact with, the membrane (it was placed on the feed wall opposite the membrane – the stiffness of the shim allowed it to keep its position away from the membrane surface without the need for a spacer). Several configurations with different thermal conducting layers were tested (Fig. 2c-f). Simulated concentrated solar heat was provided by a cartridge heater with an internal temperature sensor (McMaster-Carr, Los Angeles, CA); heat output from the heater was controlled by a thermal stat (Inkbird, Shenzhen, China). To couple the heater to the thermal carriers (mesh and shim), the thermal carriers were wrapped around the heater, with fiberglass insulation packaged around the entire assembly to minimize heat losses (Fig. 2b).

Experiments were performed to evaluate the variation of system behavior when treating high salinity feed (100 g/L NaCl) within the following range of operating conditions:

- System configuration (mesh only on the feed side, shim only on the feed side, mesh only on the distillate side, shim on the feed side and mesh on the distillate side)
- Heat source temperature (20 °C, 140 °C, 240 °C, 350 °C, 420 °C)
- Distillate absolute pressure (0.01 bar, 0.04 bar, 0.1 bar)
- Feed crossflow velocity (4 cm/s, 10 cm/s, 16 cm/s)

For each set of experiments, the distillate flux was calculated using the slope of the linear regression of the feed mass change over time, divided by the effective membrane area. Under each set of conditions, flux data were collected for at least 2 h after the system stabilized.

2.3. Characterization of Al shim and mesh

The thermally conducting metallic layers were characterized to evaluate potential corrosion after long-term use in high salinity

solutions at elevated temperature. Their surface morphologies were analyzed using scanning electron microscopy (SEM) (Zeiss Supra 40 VP, Carl Zeiss Microscopy LLC, NY). For that purpose, samples were secured on SEM stubs using double-sided carbon tape before imaging. Quantitative analysis and surface elemental mapping were also carried out using energy-dispersive X-ray spectroscopy (EDAX), which is a module included with the Zeiss Supra SEM.

2.4. Energy performance

In a typical VMD system, the energy requirements include [26]: (i) the thermal energy needed to vaporize feed water; (ii) the electrical energy required to create vacuum; and (iii) the electrical energy needed to circulate the feed. In a well-insulated VMD system, thermal energy is the largest energy component, increasing sharply with increasing feed temperature [26]. The evaluation of the energy consumption of an MD system is based on the quantities of energy consumed and the quantity of treated water. We chose specific energy consumption (SEC), a commonly used parameter, to evaluate process performance [38]. Another performance indicator, gained output ratio (GOR), of this system is defined, and investigated based on the impact of operating conditions (see Section S4 in SI).

To quantify the heat flux delivered to the membrane module by the thermal carriers, the thermal conductivity of the thermally conducting layer, k_{eff} (W/m·K), was measured (see Section S1 in SI), with $\dot{Q}_{heat}$ estimated by

$$\dot{Q}_{heat} = -k_{eff} A \frac{\Delta T}{\Delta x} \tag{3}$$

where A (m^2) is the cross-sectional area of the thermally conducting layer, ΔT (K) and Δx (m) are the temperature difference and the distance between two specified points on the thermally conducting layer along the direction of heat transfer, respectively. In this study, type K thermocouples (AWG 24 with Kapton insulation, Minnesota Measurement Instruments LLC, Minnetrista, MN) were taped to the Al shim and Al mesh surface to monitor temperature and obtain temperature gradient $\frac{\Delta T}{\Delta x}$ (K/m).

SEC (kJ/kg) is defined as the amount of total energy supplied (heat and electrical energy in this case) to produce a unit mass of pure water, which can be calculated as [39]:

$$\mathrm{SEC} = \mathrm{STEC} + \mathrm{SEEC} \tag{4}$$

where STEC (kJ/kg) is the specific thermal energy consumption, or the specific heat consumption, which can be calculated as [40],

$$\mathrm{STEC} = \frac{\dot{Q}_{heat}}{\dot{m}_{per}} \tag{5}$$

and SEEC (kJ/kg) is the specific electrical energy consumption defined as the amount of electrical energy consumed ($\dot{E}$, kJ/s) to produce a unit mass of pure water [41]:

$$\mathrm{SEEC} = \frac{\dot{E}}{\dot{m}_{per}} \tag{6}$$

The electrical energy consumption is composed of the energy needed to induce vacuum on the distillate side and to circulate the feed. Thus, the rate of electrical energy input $\dot{E}$ (kJ/s) is calculated as [42],

$$\dot{E} = \dot{E}_{vac} + \dot{E}_{cir} \tag{7}$$

$$\dot{E}_{vac} = \frac{3.35 \times 10^{-3}}{\eta_{vac}} T_p q_0 \ln\left(\frac{P_{atm}}{P_{vac}}\right) \tag{8}$$

$$\dot{E}_{cir} = \frac{\dot{V}_f \Delta P}{\eta_{cir}} \tag{9}$$

where, $\dot{E}_{cir}$ (kJ/s) and $\dot{E}_{vac}$ (kJ/s) are the rate of electrical energy consumption of the feed flow pump and the vacuum pump, respectively; η_{cir} and η_{vac} are the efficiency of feed and vacuum pump, respectively; $\dot{V}_f$ (m^3/s) is the volumetric flow rate of the feed solution; ΔP (Pa) is the feed bulk pressure difference between the inlet and outlet; T_p is the permeate temperature (K), and q_0 (L/min) is the flow rate of the gas (e.g., water vapor, leaking air) to be evacuated from the permeate line. P_{atm} (Pa) and P_{vac} (Pa) are the atmospheric and vacuum pressures, respectively [42].

3. Results and discussion

3.1. Thermal carrier and heat input

Unlike conventional VMD processes, where the feed stream is heated before entering the cell, feed solution was pumped directly to our heated VMD system at ambient temperature. Therefore, the only thermal energy input (i.e., driving force) to the system was the heat conducted by the thermal carriers. As the heat transfer efficiency between heat source and thermal conducting layer could vary depending on the form of the heat source and coupling techniques, both of which were beyond the scope of this study, we chose to calculate the heat flux that was directly delivered into the system (Fig. S1), which provides a more precise analysis of system performance given a certain heat input, regardless of heat source. Based on Eq. (3), a higher thermal conductivity of the thermal carrier, a larger cross-sectional area, or a higher temperature gradient would all contribute to a larger thermal energy input to the system, which would potentially provide a higher driving force and yield higher distillate flux. The two thermal carriers tested in this study were evaluated for their heat conducting performance. In terms of the dimensions, both Al shim and mesh had the same width, with the Al shim being 51 μm thicker than the Al mesh. The thermal conductivity of the Al shim and Al mesh were determined to be 203.4 ± 2.2 W/m·K and 20.0 ± 5.0 W/m·K, respectively. The difference in the geometries of Al shim and mesh explains the difference in their thermal conductivity – as a thin and porous material, the effective thermal conductivity of the Al mesh is only a fraction of a piece of solid Al shim. The temperature gradient on the thermal carrier is related to both the thermal conductor and the heat source temperature (for details on the specific temperatures measured on the shim and mesh, see temperature profiles in the SI (Fig. S2)). For example, when the heat source temperature was set to 140 °C, the temperature gradient on the Al shim and mesh were determined to be 25.6 ± 3.6 K/cm and 57.9 ± 13.0 K/cm, respectively.

Although the temperature gradient on the Al mesh is twice that on the Al shim, the thermal conductivity of the Al mesh is only ~10% that of the Al shim. Therefore, the overall thermal energy delivered by the Al mesh is smaller than that delivered by the Al shim. In the case of a heat source temperature of 140 °C and 240 °C, the temperature gradient on the Al mesh was 57.9 ± 13.0 K/cm and 98.1 ± 22.3 K/cm, respectively. For the configurations including shim as the thermal carrier, 140 °C was determined to be the highest possible temperature at the heat source, as higher temperatures melted the acetal flow cell. However, the lower thermal conductivity of the mesh allowed far higher temperatures to be applied to it, with temperatures as high as 420 °C being tolerated. The temperature range studied here is higher than typical MD systems because this VMD system is intended to couple with a solar collection system and conduct solar thermal heat to drive the MD process. These temperatures are well within the temperature levels that can be achieved by solar thermal collectors [43,44].

Based on the measured temperature profiles (Fig. S2), the thermal input applied in all the scenarios were calculated (Fig. 3 and Fig. S7). The results indicated that the Al shim, which has the higher thermal conductivity, delivered more heat into the system than the Al mesh, given the same heat source temperature. In addition, higher heat source temperatures helped to deliver more heat with the same thermal carrier.

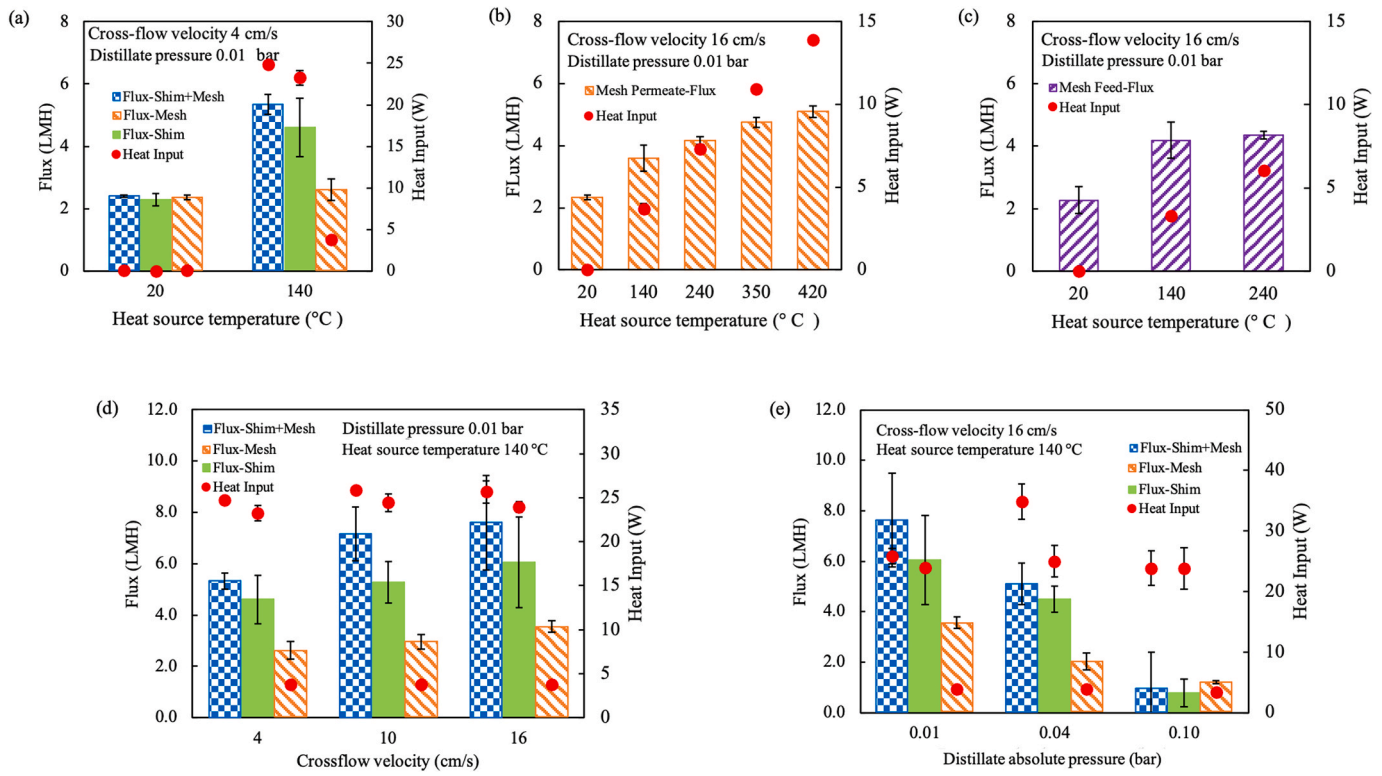

Fig. 3. Heat input and corresponding vapor flux and in 2 h long tests with different system configurations as indicated in the figures: only shim in the feed stream, only mesh in the feed stream, only mesh on the distillate side, or only shim in the feed stream and only mesh on the distillate side as the thermal carrier(s). All tests were performed with feed water contains 100 g/L NaCl. Measured water flux values are shown in bars (values correspond to the y-axis on the left) as a function of (a)–(c) temperature, (d) crossflow velocity, and (e) distillate pressure, at the conditions specified. The heat input values are shown in red dots (values correspond to the y-axis on the right). (For interpretation of the references to colour in this figure legend, the reader is referred to the Web version of this article.)

3.2. *Water flux*

The driving force for the desalination process is a partial vapor pressure difference across the membrane, which is affected by both heat and vacuum. The effect of heat and vacuum on the overall system performance were tested, and the results are shown in Fig. 3a. In these experiments, the distillate pressure was fixed at 0.01 bar and the crossflow velocity was kept at 4 cm/s. When heat was applied to the system by connecting the thermal carrier(s) to a cartridge heater operating at 140 °C, the system showed the highest flux (5.33 ± 0.32 LMH) with the shim + mesh configuration, followed by the shim-only configuration (4.6 ± 0.94 LMH), and then mesh-only on the distillate stream configuration (2.6 ± 0.35 LMH). When the heater was turned off (represented by the 20 °C bars in Fig. 3a), the flux declined to approximately 2 LMH, regardless of the thermal carrier configuration. The differences in water vapor flux between the heated and non-heated sets indicate effective heat delivery into the system through the thermal carriers, under certain conditions.

The results from the heated set suggest that higher heat input increases the flux, which is expected. When the heat source temperature is constant, the shim + mesh configuration was able to deliver the highest amount of heat among all the configurations (Fig. 3a), likely due to the extra thermal carrier compared to a single thermal carrier configuration. In the scenarios where only one thermal carrier was used, the shim delivered more heat (24.3 ± 0.8 W) than the mesh (3.7 ± 0.3 W) because of its higher thermal conductivity.

To further evaluate the change of vapor flux as a function of heat input, additional sets of experiments were conducted for the case when only the mesh was used as the thermal carrier. As shown in Fig. 3b (mesh on the distillate side), as the heat source temperature increased from 20 °C to 420 °C (corresponding to an increase of the heat input from 0 to 13.9 ± 0.1 W), the distillate flux increased from 2.3 ± 0.1 LMH to 5.1 ± 0.2 LMH. Similarly, in Fig. 3c (mesh on the feed side), the distillate flux increased from 2.3 ± 0.4 LMH to 4.3 ± 0.1 LMH as the heat source temperature increased from 20 °C to 240 °C (corresponding to an increase of heat input from 0 to 6.0 ± 0.2 W). Between these two surface heating configurations where mesh was the only thermal carrier, the flux showed no significant difference between placing the mesh on the feed or distillate side (Fig. 3b and c), which indicates that surface heating can be achieved with mesh on the distillate as effectively as placing the mesh in the feed stream. The reason for this is likely that while the PP membrane has poor thermal conductivity (0.11–0.2 W/m K) [45], the membrane's small thickness still allows ample heat to reach the membrane/water interface when it is applied to the mesh in the distillate stream. When heat is added to the mesh while it is immersed in the feed stream, it is also possible that the heat rapidly dissipates (i.e., it is carried away by the water), leading to uneven heat distribution across the membrane surface; this phenomenon is captured in our modeling effort, and described below. Considering that placing the mesh in the warm saline feed can lead to corrosion (see SI Section S3), the configuration of mesh in the feed stream was not investigated further and the rest of the discussion will focus on the results from other configurations (Fig. 2d-f).

In the series of experiments conducted to determine the impact of the crossflow velocity on the membrane flux, we observed that the flux increases as crossflow velocity increased for all system configurations (Fig. 3d). Some conventional MD systems showed similar behavior, and this phenomenon was attributed to the decrease in temperature polarization as crossflow velocity increases [3,7]. Our numerical analysis (Section 3.4) also supported that; in these tested conditions higher feed velocity helped to reduce the impact of temperature polarization, thus increasing vapor flux. This result is highly beneficial because it allows

the system to operate at crossflow velocities that can minimize membrane fouling while still taking advantage of surface and feed-stream heating with enhanced flux. It is likely that in a longer membrane module the flow velocity would further strengthen the impact on flux, as any heat not used for flux generation would be carried further down the module, increasing the bulk fluid temperature, and increasing water flux. Therefore, the results in Fig. 3d represent a lower bound on flux, with longer modules likely leading to higher fluxes, given a certain level of heat input (see section 3.4 for more data and discussion).

In the set of experiments used to determine the impact of distillate vacuum pressure on membrane flux, the heat source temperature and cross-flow velocity were fixed while different vacuums were applied (Fig. 3e). Regardless of the configuration, lower distillate pressure (i.e., higher vacuum level) lead to higher flux, with the vapor flux being highly sensitive to vacuum pressure, and flux dropping substantially (from ~8 LMH to ~1 LMH) when the distillate pressure increased from 0.01 bar to 0.10 bar. These trends can be explained by the fact that flux is proportional to the vapor pressure difference between feed side and distillate side, shown as

$$J = A_m\left(P_{m,f} - P_v\right) \tag{10}$$

where J is the distillate flux, A_m is the membrane permeability, $P_{f,m}$ is the partial vapor pressure at feed/membrane interface, P_v is the absolute pressure on the distillate side. $P_{m,f}$ is determined by the temperature at the feed/membrane interface $T_{m,f}$ (K), which can be expressed in Antoine Equation [46],

$$P_{m,f} = \left(\frac{1}{1+m}\right)\exp\left(23.1964 - \frac{3816.44}{T_{m,f} - 46.13}\right) \tag{11}$$

where m is the molar fraction of salt at the feed/membrane interface. The increase of distillate pressure (P_v) directly impacts the flux.

In all the experiments, it can be concluded that the shim + mesh configuration, which yields the highest flux, achieved this elevated performance because of the shim's ability to deliver larger amounts of heat to the system. However, the heat use efficiency, i.e., the efficiency at which this heat is converted to vapor, was highest with the mesh-only configuration, which is explored further below in Section 3.3. In all experiments and configurations, salt rejection was higher than 99.9% throughout the entire experimental process.

3.3. System energy performance

When evaluating the system performance of an MD process, distillate flux is an important criterion (used to determine the needed membrane area, and more generally the capital costs of the system), but it is also critical to consider the energy needed to drive the process (typically, a major component of the operating expenses). The energy performance of the system under different operating conditions in terms of GOR and SEC was investigated. SEC is determined by both energy consumption and distillate flux. Among the three operating variables, thermal energy

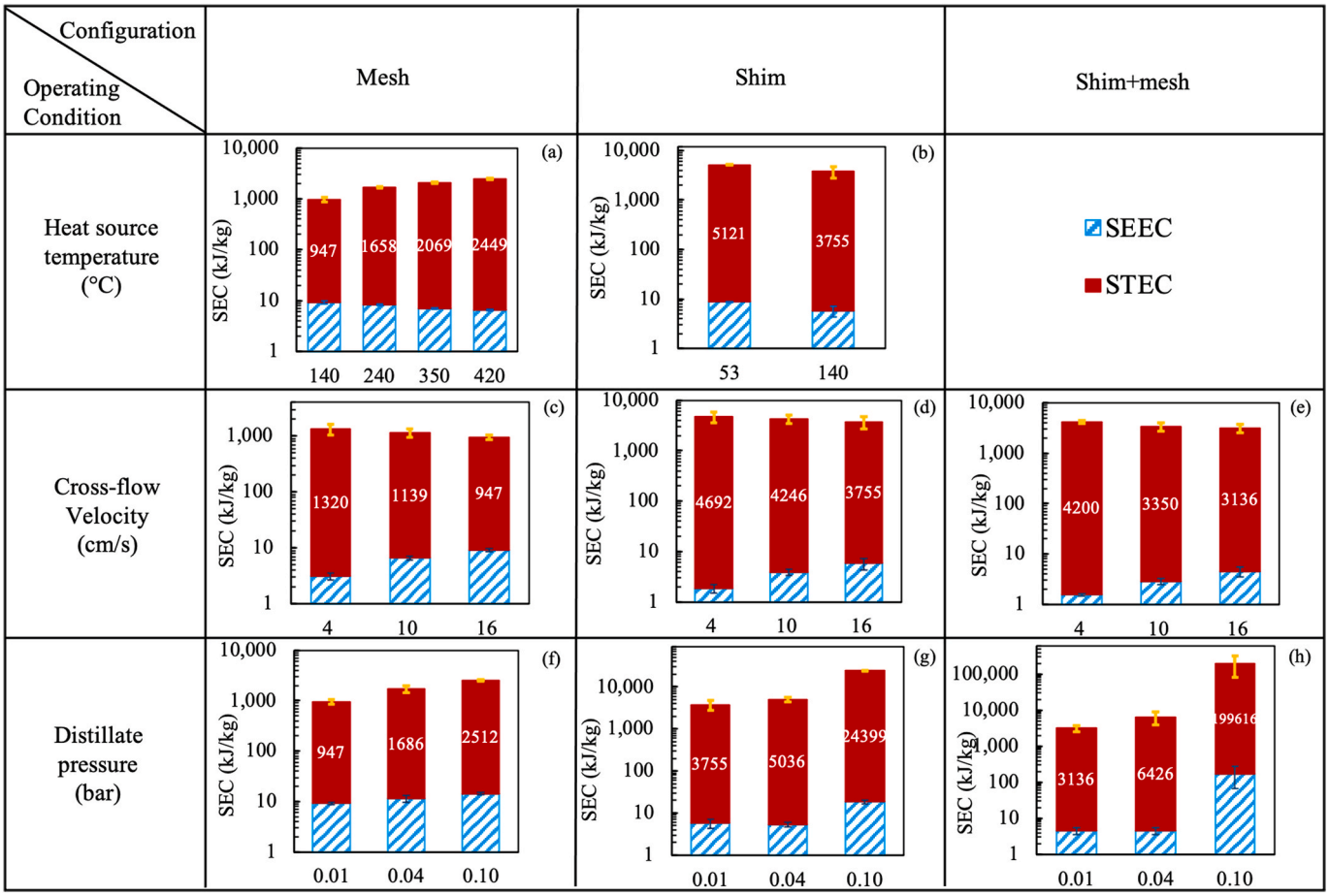

Fig. 4. SEC of 2h long vacuum membrane distillation tests with different system configurations as indicated in the figures: only shim in the feed stream, only mesh on the distillate side or both shim in the feed stream and mesh on the distillate side as the thermal carrier(s). All tests were performed with feed water contains 100 g/L NaCl. Regarding the operating conditions, unless specified as the variable, the heater temperature was set as 140 °C, cross-flow velocity was fixed at 16 cm/s and the distillate pressure was kept at 0.01 bar. The blue hatch bar represents the value of SEEC and the red solid bar represents the value of STEC. The SEC value is the sum of SEEC and STEC (the total bar height) as shown in the figures.

consumption is strongly associated with heat source temperature and is hardly affected by cross-flow velocity and distillate pressure. In contrast, the electrical energy consumption is dominated by the pumping rate (i.e., the cross-flow velocity) and vacuum pressure.

The impact of the heat source temperature (i.e., thermal energy input) on the system's SEC is shown in Fig. 4a and b. Specifically, in Fig. 4a, in the heat source temperature range of 140 °C–420 °C, which corresponds to a total heat input to the system of ~3.8 W–~13.9 W, the STEC increased from 947 to 2449 kJ/kg. The results in Fig. 3b indicate that vapor flux increased with increasing heat input; however, the flux increase rate was slower than the thermal energy input increase rate. As a result, the cost of the elevated vapor flux with higher thermal energy input is an increase in STEC. In contrast, in Fig. 4b, the flux increase rate was faster than the thermal energy input increase rate, which leads to a decrease in STEC. However, at the same operating temperature of 140 °C, STEC of shim-only configuration (3755 kJ/kg) is higher than that of mesh-only configuration (947 kJ/kg); increasing the shim temperature beyond 140 °C was not possible due to damage to the plastic membrane housing. This demonstrates that based on STEC, mesh heating is more efficient than shim heating; under the given operating conditions, lower thermal input is more favorable in terms of thermal energy efficiency, albeit with other costs associated with lower flux operation (i.e., larger membrane surface area and capital cost to treat a given volume of contaminated water). A decrease in SEEC was observed as the heat source temperature increased simply because the flux (denominator) increased (Fig. 4a and b). Electrical energy consumption in the system is associated with the electricity needed to operate the vacuum and circulation pumps, neither of which had changed substantially as the heat input increased. Because STEC is approximately 3 orders of magnitude higher than SEEC, the net change of STEC and SEEC (i.e., the overall SEC) increased as heat input to the system increased. For example, the SEC value is approximately 2.5 times greater at 420 °C compared to 140 °C (heat source temperature) for the mesh-only configuration.

The effect of crossflow velocity on the system energy performance in terms of SEC are shown in Fig. 4c-e. For all tested configurations, the overall SEC decreased with increasing crossflow velocity. When crossflow velocity increases, the thermal energy input to the system is not affected substantially, whereas there is a slight increase in electrical energy consumption from the recirculation pump. However, the addition of small amount of electrical energy input (due to circulating the feed at a higher velocity) brought much higher flux as a benefit, which is reflected in the SEC values. Overall, the SEC of the system was lowered by the increase in crossflow velocity. Specifically, when the crossflow velocity increased from 4 to 16 cm/s, SEC deceased by 26.5 ± 8.7%, 20.5 ± 6.6%, 25.3 ± 14.1%, for the mesh, shim, and shim + mesh configurations, respectively. Among the three configurations, the mesh-only configuration showed the lowest SEC (947–1320 kJ/kg depending on the crossflow velocity, with a flux range of 2.6–3.5 LMH), followed by shim + mesh configuration (3136 to 4200 kJ/kg, with a flux range of 5.3–7.6 LMH), and shim only configuration (3735 to 4692 kJ/kg, with a flux range of 4.6–6.0 LMH). This demonstrates the advantage of providing heat directly to the membrane surface in terms of minimizing specific energy consumption of the system, although the most energy efficient system tends to deliver the least water flux.

Fig. 4f-h demonstrate the effects of the vacuum pressure on system SEC. For all tested configurations, SEC increased with increasing distillate absolute pressure. While the thermal energy input to the system was not affected when distillate pressure increased (i.e., vacuum depth decreases), the electrical energy required to induce vacuum should be lower when the vacuum pump needs to maintain a lower vacuum. While the energy consumption did not change much, the vapor flux decreased substantially when the distillate pressure was higher. Thus, both STEC and SEEC increased substantially as a result of increase in distillate absolute pressure. To achieve the lowest SEC (both STEC and SEEC) values and highest flux, the pressure on the distillate side should be maintained as low as possible. Of the three configurations tested, the mesh-only configuration exhibits the smallest SEC (947–2512 kJ/kg) with lowest flux (1.1–3.5 LMH). The shim + mesh configuration that generates the highest flux (0.9–7.6 LMH) was the least energy efficient with a high SEC range of 3136 to 199616 kJ/kg. Again, the results demonstrate the advantage of providing heat to the membrane surface, compared to heating the bulk stream in terms of energy efficiency, but with reduced water productivity.

The flux and energy performance of different MD systems, including data from this study (blue squares, grey triangles, and yellow circles) and others [17,23,39,47–65] (orange diamonds) are summarized in Fig. 5. As shown in Fig. 5, the 48 STEC values from cited references fluctuate substantially over 3 orders of magnitude. The broad range of STEC from different systems indicates that STEC is sensitive to system characteristics and operating parameters, which also implies a great potential for STEC improvement in most MD processes. In general, systems that include a surface heating element demonstrated the lower STEC values, which shows the important role that surface heating plays in increasing system energy efficiency [27,28]. It further stresses the importance of identifying the right location for incorporating the heat conducting element into a VMD system. Compared to other studies, the STEC values from this study are on the lower side. However, this low STEC is achieved at the cost of low flux. Note that the lowest STEC values in Fig. 5 have been recorded in surface heating (mesh only configuration) VMD settings with the water flux performance at the lower end (less than 5 LMH). When heat conducted through mesh is the only means of heat input, the thermal energy delivered to the system is limited and vacuum makes an important contribution to the generated flux. In these scenarios, a low thermal energy input could deliver reasonable flux with the assistance from the vacuum (i.e., increased electrical energy consumption), and the STEC values appear to be lower. When membrane heating was combined with bulk feed heating (the shim + mesh configuration), the flux is higher, but the SEC of the system increased. Flux is related to the membrane area needed to achieve a certain water treatment rate. Low flux systems, by definition, require larger surface areas, which translates into higher capital costs. In contrast, the SEC (STEC as the major component) determines the operational cost of the system. Therefore, it is important to evaluate both flux performance and

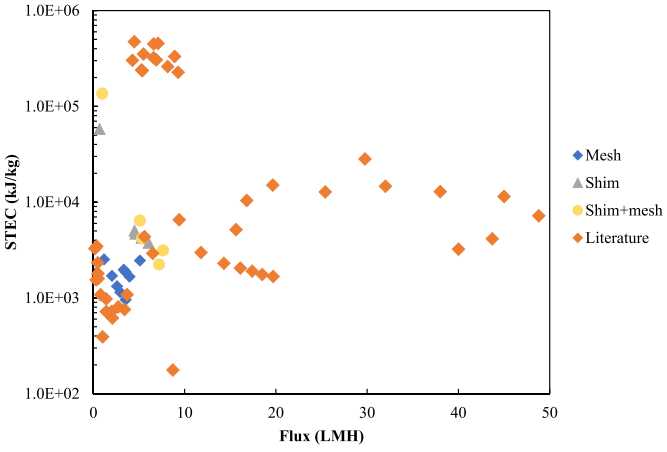

Fig. 5. Comparison of performance of different membrane distillation systems, including STEC (thermal energy performance) and flux (water productivity). Feed temperature data are available in Table S3 in SI. The orange diamonds represent the data from literature [17,23,39,47–65]. The blue squares, grey triangles and yellow circles represent the data from the direct heating MD experiments with mesh only configuration, shim only configuration, and shim + mesh configuration from this study, respectively. Higher flux indicates better water production and lower STEC values indicate higher thermal energy efficiency. (For interpretation of the references to colour in this figure legend, the reader is referred to the Web version of this article.)

energy performance of a system and balance the tradeoff between membrane flux and SEC, to minimize the overall cost.

The direct heating MD system presented here is different from conventional MD systems where the driving force for desalination is delivered through the feed stream. When heat is delivered to where it is needed (i.e., the membrane/water interface), it only requires a minimal amount of thermal energy input because the heat at the interface can be more effectively used for evaporation, particularly with vacuum assistance. However, increased efficiency comes at a cost of lower flux. Therefore, when considering the application of these systems, the efficiency of energy consumption must be balanced with increased capital expenses.

3.4. Numerical analysis

We complement our experimental measurements with a numerical model that simulates steady-state heat transport and vapor production in the VMD system sketched in Fig. 6. A feed channel of length L, height H, and width W is bounded by thermally insulated walls at $z = \pm W/2$ and $y = H$. The feed channel is bounded at $y = 0$ by a hydrophobic membrane of thickness δ_1, overlying a metallic mesh of thickness δ_2. We neglect concentration polarization, and assume pure water enters the channel at $x = 0$ with a uniform temperature T_{in} and mean velocity U_{in}. Steady heat transport in the channel is governed by the thermal energy equation,

$$\nabla(\mathbf{u}T) = \alpha_f \nabla^2 T \tag{12}$$

where T, $u = [u, v, w]$, and α_f are the feed temperature, velocity vector, and thermal diffusivity, respectively. We assume incompressible feed flow and neglect variations of α_f with temperature. We evaluate α_f using T_{in}. Though ongoing work in our group includes simulation of the Navier-Stokes equation in the feed channel, we present here a simpler model that approximates the feed velocity as

$$u(x,y,z) \approx u_d(y,z),\ v(x,y,z) \approx v_m(y,z),\ w = 0 \tag{13}$$

where the downstream velocity $u_d(y,z)$ is the analytical solution for fully-developed laminar duct flow [66], and $v_m(y,z)$ is the feed velocity normal to the membrane, evaluated at the membrane surface, $y = 0$. This approximation reduces CPU time and leverages the fact that v is typically four orders-of-magnitude smaller than U_{in}, such that downstream variations of $u(x,y,z)$ are very small. Furthermore, the membrane-normal velocity v primarily impacts heat transport in a thermal boundary-layer at the membrane surface. Satisfaction of the no-slip and no-penetration conditions for v on the impermeable walls is consequently of secondary importance. Note that our model captures variations of the feed temperature and vapor flux over the membrane surface.

We apply the following temperature boundary conditions in the feel channel,

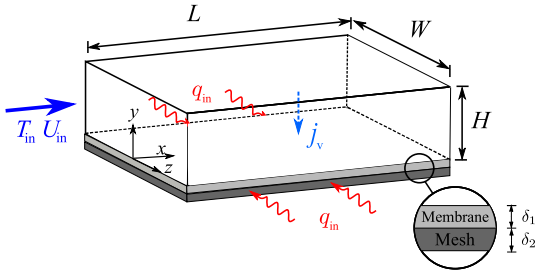

Fig. 6. Illustration (not to scale) of the geometry considered by our numerical analysis.

$$T|_{x=0} = T_{in},\ \left.\frac{\partial T}{\partial z}\right|_{z=\pm W/2} = \left.\frac{\partial T}{\partial y}\right|_{y=h} = \left.\frac{\partial^2 T}{\partial x^2}\right|_{x=L} = 0 \tag{14}$$

We model vapor transport through the composite membrane using the Schofield model [67], which assumes the transmembrane mass flux j satisfies Eq. (10) where the vapor pressure $P_{m,f}$ at the membrane feed surface ($y = 0$) is computed using Eq. (11).

As detailed in Section S5 in the Supporting Information, heat transport in the membrane and mesh layers can be modeled using the volume-averaged equation,

$$\frac{\partial}{\partial y}\left(Tc_{p,v}j_v\right) = k_i \nabla^2 T, \quad k_i = \varphi_i k_v + (1-\varphi_i)k_{s,i} \tag{15}$$

where $c_{p,v}$ is the specific heat at constant pressure of the vapor, k_i is an effective thermal conductivity, φ_i is the porosity, and k_v and $k_{s,i}$ are the thermal conductivities of the vapor and solid phases, respectively. The subscript $i = 1, 2$ is used to distinguish between the properties evaluated in the membrane layer ($i = 1$) or underlying mesh ($i = 2$).

Conservation of energy [68] requires the following conditions at the feed-membrane interface,

$$T|_{y=0^+} = T|_{y=0^-},\quad k_f \left.\frac{\partial T}{\partial y}\right|_{y=0^+} - k_1 \left.\frac{\partial T}{\partial y}\right|_{y=0^-} = j\lambda \tag{16}$$

where $\lambda = -2{,}438T + 250{,}300$ is the latent heat of water vaporization, assuming T and λ have units °C and kJ/kg, respectively. This relation was derived using the OLI Stream Analyzer database. The superscripts + and - denote evaluation of T at the feed and membrane side of the interface, respectively. Conservation of energy at the interface between the membrane and mesh requires,

$$T|_{y=\delta_1^+} = T|_{y=\delta_1^-},\ k_1 \left.\frac{\partial T}{\partial y}\right|_{y=\delta_1^+} = k_2 \left.\frac{\partial T}{\partial y}\right|_{y=\delta_1^-} \tag{17}$$

On the inlet, outlet, and lower surface of the composite membrane, we assume negligible conductive heat transport,

$$\left.\frac{\partial T}{\partial x}\right|_{x=0} = \left.\frac{\partial T}{\partial x}\right|_{x=L} = \left.\frac{\partial T}{\partial y}\right|_{y=-\delta_1-\delta_2} = 0 \tag{18}$$

Note that thermal energy nevertheless exits the system through the membrane due to advection. On the side walls $z = \pm W/2$, we assume the membrane layer is thermally insulated,

$$\left.\frac{\partial T}{\partial z}\right|_{z=\pm W/2} = 0,\ -\delta_1 < y < 0 \tag{19}$$

while heat enters the system through the mesh,

$$k_2 \left.\frac{\partial T}{\partial z}\right|_{z=\pm W/2} = q_{in},\ -\delta_1 - \delta_2 < y \le -\delta_1 \tag{20}$$

All equations are discretized spatially using second-order finite-volume methods coded in-house with Fortran [69,70]. The code was verified against analytical solutions and validated against experimental data, as detailed in Dudley [71] and demonstrated by Lou et al. [70]. We also performed mesh-independence studies to ensure a relative truncation error on the order of 1%. Fig. 7 demonstrates our validation, in which we compare the vapor flux predictions of our model to those measured by our bench-scale system. For that purpose, we set the model dimensions ($L = 10$ cm, $W = 4$ cm, and $H = 4$ mm), membrane properties ($\varphi_1 = 0.85$, $\delta_1 = 100$ μm, $k_{s,1} = 0.11$ W/m-K), and mesh properties ($\varphi_2 = 0.27$, $\delta_2 = 203.2$ μm, $k_{s,2} = 200$ W/m-K) to those of the experimental system. Note that the thermal conductivities of the membrane and mesh are set to those of polypropylene and aluminum, respectively. We also modified the numerical model to apply heat to only side of the membrane, consistent with experiments. Experiments and simulations were then performed for the combinations of heat inputs q_{in}, inlet

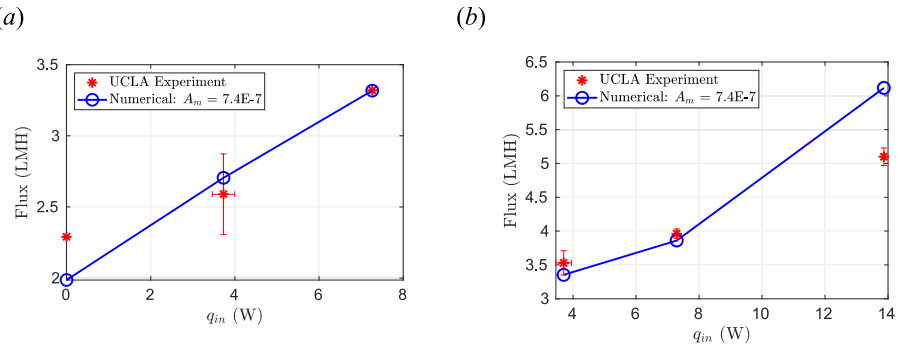

Fig. 7. Comparison of experimental (red asterisks) and numerical (blue circles) measurements of vapor flux as a function of q_{in} for (a) experiments labeled 1–3 in Table 1, (b) experiments labeled 4–6 in Table 1. (For interpretation of the references to colour in this figure legend, the reader is referred to the Web version of this article.)

temperatures T_{in}, and flow rates U_{in} summarized in Table 1, for the constant vacuum pressure P_{vac} = 0.01 bar. As heat input can vary depending on the thermal conducting layer material and dimension, the heat source type and temperature, and system configuration, the heat input q_{in} was chosen as a normalizing factor in the simulation studies. The flow was heated using only the mesh, i.e. without the heated shim.

Fig. 7(*a*) compares our experimental (red asterisks) and numerical (blue circles) results for the average transmembrane vapor flux as a function of q_{in} for the experiments labeled 1–3 in Table 1. These were conducted for the relatively slow feed velocity $U_{in} = 4.06$ cm/s. Note the reported value of T_{in} from Table 1 represents the average feed temperature throughout the entire experiment; the increase in T_{in} with q_{in} is explained by the recycling of the concentrate in the experimental system. The only model parameter not known *a-priori* is the membrane vapor permeability A_m. For that purpose, we performed a large suite of simulations for different values of A_m, and found that $A_m = 7.4 \times 10^{-7}$ kg/m s Pa provided the best fit to the experimental data in Fig. 7(*a*), producing a mean percentage error of 5.9%. This permeability is roughly 25% lower than those reported by Vanneste et al. [72] and Lou et al. [70], who report $A_m = 10^{-6}$ and 1.87×10^{-6} kg/m s Pa, respectively, for the same membrane material in a direct contact MD system. The difference likely arises because our permeability is an effective value for both the membrane and underlying mesh material. Having determined A_m, we then compared experimental and numerical results for the experiments labeled 4–6 in Table 1, which were performed for the larger feed velocity $U_{in} = 16.3$ cm/s. Fig. 7(*b*) shows that in this case, our model agrees with the experiments to within 9.2% mean percentage error. An additional validation of our numerical model for cases with a heated shim are provided in Supporting Information (Section S6). With the successful model validation using experimental results from different operational conditions, parametric studies were performed to predict system performance in a larger-scale flow cell. These simulation results serve as guidance of the optimization of operational conditions in a scaled-up system with minimal experiments.

To explore heat transport and vapor production in a larger VMD system, we perform a parametric study for a system of dimensions $L = 1$ m, $W = 8$ cm, and $h = 2$ mm and a constant inlet feed temperature of T_{in} = 30 °C. We assume that vacuum evacuates all the vapor and maintains a constant driving force on the distillate side. All properties of the composite membrane were set to those of the experimental system, with the exception of the mesh thickness, which was rounded down to δ_2 = 200 μm. We then varied the heat input between $0 \leq q_{in} \leq 400$ W, considering a larger system might require higher heat input compared to the bench-scale system. We studied the feed velocity between $1 \leq U_{in} \leq 10$ cm/s, which is a practical velocity range during membrane operations – high enough to contribute to membrane fouling control, but not too high so as to substantially increase operational costs. Heat was applied to both lateral edges of the mesh, i.e. at $z = \pm W/2$.

Table 1
Operating conditions used for experiments and simulations presented in Fig. 7.

Exp #	1	2	3	4	5	6
q_{in} (W)	0	3.73	7.26	3.70	7.29	13.9
T_{in} (°C)	16.8	18.4	19.5	20.2	21.0	25.7
U_{in} (cm/s)	4.06	4.06	4.06	16.3	16.3	16.3

To investigate the impact of mesh heating (q_{in}), we begin by setting U_{in} = 10 cm/s and q_{in} = 20 W. Fig. 8(*a*) shows the resulting cross-sectional temperature profiles on the membrane surface ($y = 0$) at the downstream locations $x = L/4$ (solid line), $L/2$ (dashed line), and L (dash-dotted line). The highest temperatures occur near the lateral walls, where the heating is applied. For this small value of q_{in}, we see that the maximum temperature is always below the inlet value, T_{in} = 30 °C, and also decreases with downstream distance. This occurs because the low heat input does not match that lost to evaporation. Fig. 8(*b*) shows the corresponding results when the heating is increased to $q_{in} = 400$ W. The maximum temperature is now always above the inlet value, reaching T = 55 °C at the outlet. The maximum temperature also increases with downstream distance. Meanwhile, the lowest membrane temperatures occur in the middle of the membrane, and remain near the inlet value $T_{in} = 30$ °C. We conclude that for this high heating value, q_{in} exceeds the heat lost to evaporation, such that temperature polarization is not only removed, but actually reversed. We also observe that the temperature profiles suddenly flatten near the lateral walls at $z = \pm W/2$. This is an artifact of our discretization of the thermally insulated boundary conditions.

To explore the impact of heating on local vapor production, we define the width-averaged flux

$$j_w(x) = \frac{1}{W} \int_{-W/2}^{W/2} j_v(x, z)\, dz \tag{22}$$

Fig. 8(*c*) shows the downstream variation of $j_w(x)$ when $U_{in} = 10$ cm/s and $q_{in} = 20$ W (solid line) and $q_{in} = 400$ W (dashed line). We see that for $q_{in} = 20$ W, the vapor flux decreases with downstream distance due to temperature polarization. In contrast, when $q_{in} = 400$ W, we see $j_w(x)$ increases with downstream distance. An additional series of simulations found that when $q_{in} = 201$ W, the width-averaged flux j_w (x) is constant, as demonstrated by the dash-dotted line in Fig. 8c. For active heating above this threshold value, the single-pass recovery of the heated VMD system can be increased by simply increasing the system length, without suffering from downstream heat loss due to temperature polarization.

Fig. 8(*d*) shows the net vapor flux as a function of q_{in} when $U_{in} = 10$ cm/s (asterisks) and U_{in} = 1 cm/s (circles). We see that for heating values below around q_{in} = 250 W, the higher feed velocity produces more net flux. That occurs because the heating is not sufficient to completely reverse the effects of temperature polarization. In that case, a

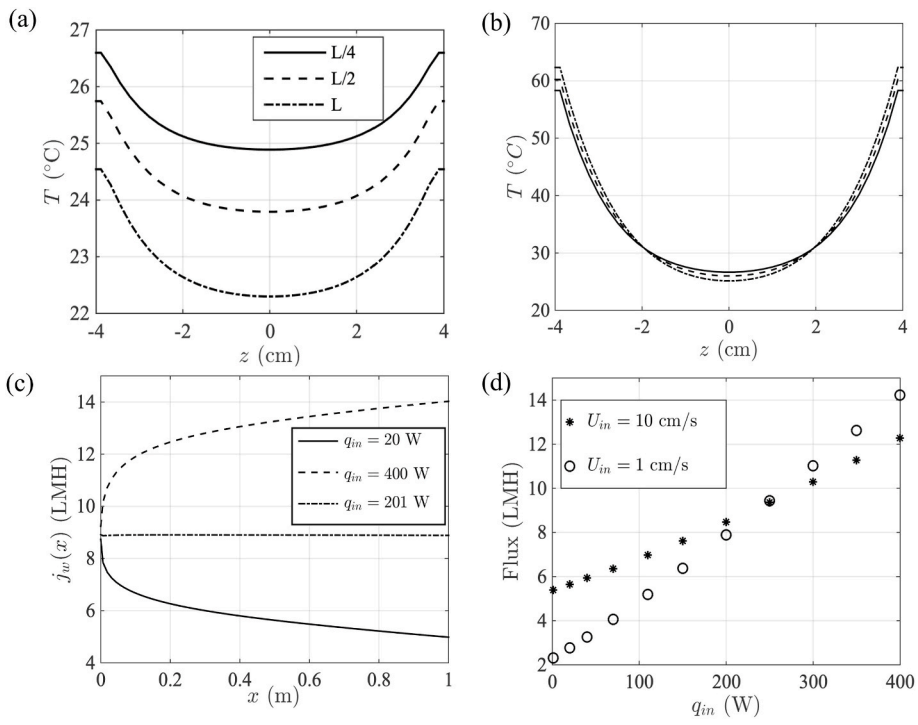

Fig. 8. (a) Temperature profiles on the membrane surface ($y = 0$) at the downstream locations $x = L/4$ (solid line), $L/2$ (dashed line), and L (dash-dotted line) when $q_{in} = 20$ W and $U_{in} = 10$ cm/s. (*b*) Corresponding temperature profiles when $q_{in} = 400$ W and $U_{in} = 10$ cm/s. (c) Downstream variation of the width-averaged flux $j_w(x)$ when $U_{in} = 10$ cm/s and $q_{in} = 20$ W (solid line), $q_{in} = 400$ W (dashed line), and $q_{in} = 201$ W (dashed-dotted line). (*d*) Net flux as a function of q_{in} when $U_{in} = 10$ cm/s (asterisk symbols) and $U_{in} = 1$ cm/s (circles).

higher feed velocity is preferred, because it reduces the impact of temperature polarization, and increases the net flux. This likely explains our experimental observations that distillate flux increased with feed velocity. In contrast, for heating values above $q_{in} = 250$ W, the lower feed velocity produces more flux. In this case, a lower feed velocity increases the residence time of the feed passing through the channel, and allows it to heat to higher values, thereby increasing flux. When treating feed waters for which mineral scaling is not a concern, we conclude that systems can benefit from operating at a high q_{in} and a low U_{in}. For the case of high-concentration brines, one must also consider that lower feed velocities tend to exacerbate concentration polarization and mineral scaling.

We have demonstrated experimentally and numerically that the direct heating approach is capable of mitigating or even reversing temperature polarization. It is important to note that temperature and concentration polarization are coupled phenomena because they both depend on, and influence the water vapor flux through the membrane. On the one hand, the elevated membrane surface temperature helps to maximize vapor flux by maintaining the driving force and reduce some scaling by increasing the solubility of alkali metal salts (e.g., NaCl). On the other hand, high temperatures at the membrane/water interface increases vapor flux, which increases concentration polarization and reduces the solubility of certain common mineral species (e.g., $CaCO_3$ and $CaSO_4$), which increases scaling. Therefore, temperature polarization needs to be optimized to an appropriate level where flux is maximized while scaling is minimized (or at the very least kept at a tolerable level).

4. Conclusions

We developed a VMD process using layered composite membranes that include a high-thermal-conductivity layer for supplying heat directly to the membrane-water interface and throughout the flow channel. The VMD system showed stable performance over hours of desalinating hypersaline feed and exhibited water fluxes as high as 9 LMH and salt rejection >99.9%. We also investigated the impact of operational conditions on system performance. Flux was shown to be affected by heat input, feed crossflow velocity, and vacuum level, while salt rejection remained to be higher than 99.9% under all the tested conditions. Our CFD simulations were in agreement with experimental results. The numerical models developed here were able to successfully describe the transport phenomena in the system and predict the ability to use this VMD process for larger scale systems. Compared to conventional VMD systems, direct heating VMD systems demonstrated higher energy efficiency, which stresses the importance of identifying the right location for incorporating the heat conducting element into a VMD system. This process has the potential of solving several problems associated with MD-based desalination and brine concentration processes, such as minimizing heat losses, increasing thermal efficiency, and limiting the number of heat exchangers.

CRediT authorship contribution statement

Jingbo Wang: Investigation, Data curation, Methodology, Visualization, Writing – original draft. **Yiming Liu:** Investigation, Data curation, Writing – review & editing. **Unnati Rao:** Investigation. **Mark Dudley:** Investigation, Data curation, Methodology, Visualization, Writing – original draft. **Navid Dehdari Ebrahimi:** Investigation, Methodology. **Jincheng Lou:** Investigation. **Fei Han:** Investigation. **Eric M.V. Hoek:** Supervision, Writing – review & editing. **Nils Tilton:** Supervision, Writing – review & editing. **Tzahi Y. Cath:** Supervision, Writing – review & editing. **Craig S. Turchi:** Supervision, Writing – review & editing. **Michael B. Heeley:** Supervision, Writing – review & editing. **Y. Sungtaek Ju:** Methodology. **David Jassby:** Funding acquisition, Methodology, Supervision, Conceptualization, Writing – review & editing.

Declaration of competing interest

The authors declare that they have no known competing financial interests or personal relationships that could have appeared to influence the work reported in this paper.

Acknowledgements

The SEM and EDAX analyses were conducted at the California

NanoSystems Institute, Los Angeles, California, 90095, USA. This work was supported by the Department of Energy (DOE) (Award No. DE-EE0008391) and the Sustainable LA Grand Challenge (EMVH).

Appendix A. Supplementary data

Supplementary data to this article can be found online at https://doi.org/10.1016/j.memsci.2021.119188.

References

[1] M.S. El-Bourawi, Z. Ding, R. Ma, M. Khayet, A framework for better understanding membrane distillation separation process, J. Membr. Sci. (2006), https://doi.org/10.1016/j.memsci.2006.08.002.

[2] K.W. Lawson, D.R. Lloyd, Membrane distillation, J. Membr. Sci. (1997), https://doi.org/10.1016/S0376-7388(96)00236-0.

[3] A. Alkhudhiri, N. Darwish, N. Hilal, Membrane distillation: a comprehensive review, Desalination 287 (2012) 2–18, https://doi.org/10.1016/j.desal.2011.08.027.

[4] J. Wu, K.R. Zodrow, P.B. Szemraj, Q. Li, Photothermal nanocomposite membranes for direct solar membrane distillation, J. Mater. Chem. A. 5 (2017) 23712–23719, https://doi.org/10.1039/c7ta04555g.

[5] X. Chen, N.Y. Yip, Unlocking high-salinity desalination with cascading osmotically mediated reverse osmosis: energy and operating pressure analysis, Environ. Sci. Technol. (2018), https://doi.org/10.1021/acs.est.7b05774.

[6] C.K. Chiam, R. Sarbatly, Vacuum membrane distillation processes for aqueous solution treatment-A review, Chem. Eng. Process. - Process Intensif. 74 (2013) 27–54, https://doi.org/10.1016/j.cep.2013.10.002.

[7] M.A.E.R. Abu-Zeid, Y. Zhang, H. Dong, L. Zhang, H.L. Chen, L. Hou, A comprehensive review of vacuum membrane distillation technique, Desalination 356 (2015) 1–14, https://doi.org/10.1016/j.desal.2014.10.033.

[8] S. Lin, N.Y. Yip, M. Elimelech, Direct contact membrane distillation with heat recovery: thermodynamic insights from module scale modeling, J. Membr. Sci. (2014), https://doi.org/10.1016/j.memsci.2013.11.016.

[9] M. Qtaishat, T. Matsuura, B. Kruczek, M. Khayet, Heat and Mass Transfer Analysis in Direct Contact Membrane Distillation, Desalination (2008), https://doi.org/10.1016/j.desal.2007.05.019.

[10] A.S. Alsaadi, L. Francis, G.L. Amy, N. Ghaffour, Experimental and theoretical analyses of temperature polarization effect in vacuum membrane distillation, J. Membr. Sci. 471 (2014) 138–148, https://doi.org/10.1016/j.memsci.2014.08.005.

[11] G. Zuo, G. Guan, R. Wang, Numerical modeling and optimization of vacuum membrane distillation module for low-cost water production, Desalination 339 (2014) 1–9, https://doi.org/10.1016/j.desal.2014.02.005.

[12] J.P. Mericq, S. Laborie, C. Cabassud, Vacuum membrane distillation of seawater reverse osmosis brines, Water Res. 44 (2010) 5260–5273, https://doi.org/10.1016/j.watres.2010.06.052.

[13] S. Bandini, C. Gostoli, G.C. Sarti, Separation efficiency in vacuum membrane distillation, J. Membr. Sci. (1992), https://doi.org/10.1016/0376-7388(92)80131-3.

[14] S.G. Lovineh, M. Asghari, B. Rajaei, Numerical Simulation and Theoretical Study on Simultaneous Effects of Operating Parameters in Vacuum Membrane Distillation, Desalination (2013), https://doi.org/10.1016/j.desal.2013.01.005.

[15] J. Zhang, J. De Li, M. Duke, M. Hoang, Z. Xie, A. Groth, C. Tun, S. Gray, Modelling of vacuum membrane distillation, J. Membr. Sci. 434 (2013) 1–9, https://doi.org/10.1016/j.memsci.2013.01.048.

[16] M. Khayet, Solar desalination by membrane distillation: dispersion in energy consumption analysis and water production costs (a review), Desalination 308 (2013) 89–101, https://doi.org/10.1016/j.desal.2012.07.010.

[17] A. Deshmukh, C. Boo, V. Karanikola, S. Lin, A.P. Straub, T. Tong, D.M. Warsinger, M. Elimelech, Membrane distillation at the water-energy nexus: limits, opportunities, and challenges, Energy Environ. Sci. 11 (2018) 1177–1196, https://doi.org/10.1039/c8ee00291f.

[18] Y. Zhou, R.S.J. Tol, Evaluating the costs of desalination and water transport, Water Resour. Res., 2005, https://doi.org/10.1029/2004WR003749.

[19] M. Shannon, P.W. Bohn, M. Elimelech, J.G. Georgiadis, B.J. Mariñas, A.M. Mayes, Science and technology for water purification in the coming decades, Nature 452 (2008) 301–310, https://doi.org/10.1038/nature06599.

[20] P.A. Hogan, Sudjito, A.G. Fane, G.L. Morrison, Desalination by solar heated membrane distillation, Desalination (1991), https://doi.org/10.1016/0011-9164(91)85047-X.

[21] F. Banat, R. Jumah, M. Garaibeh, Exploitation of solar energy collected by solar stills for desalination by membrane distillation, Renew. Energy (2002), https://doi.org/10.1016/S0960-1481(01)00058-1.

[22] J. Koschikowski, M. Wieghaus, M. Rommel, Solar Thermal-Driven Desalination Plants Based on Membrane Distillation, Desalination (2003), https://doi.org/10.1016/S0011-9164(03)00360-6.

[23] J. Koschikowski, M. Wieghaus, M. Rommel, V.S. Ortin, B.P. Suarez, J.R. Betancort Rodríguez, Experimental Investigations on Solar Driven Stand-Alone Membrane Distillation Systems for Remote Areas, Desalination (2009), https://doi.org/10.1016/j.desal.2008.05.047.

[24] F. Banat, N. Jwaied, M. Rommel, J. Koschikowski, M. Wieghaus, Performance evaluation of the "large SMADES" autonomous desalination solar-driven membrane distillation plant in Aqaba, Jordan, Desalination 217 (2007) 17–28, https://doi.org/10.1016/j.desal.2006.11.027.

[25] J. Blanco Gálvez, L. García-Rodríguez, I. Martín-Mateos, Seawater desalination by an innovative solar-powered membrane distillation system: the MEDESOL project, Desalination 246 (2009) 567–576, https://doi.org/10.1016/j.desal.2008.12.005.

[26] J.P. Mericq, S. Laborie, C. Cabassud, Evaluation of systems coupling vacuum membrane distillation and solar energy for seawater desalination, Chem. Eng. J. (2011), https://doi.org/10.1016/j.cej.2010.11.030.

[27] C. Chen, Y. Kuang, L. Hu, Challenges and Opportunities for Solar Evaporation, Joule (2019), https://doi.org/10.1016/j.joule.2018.12.023.

[28] L. Cui, P. Zhang, Y. Xiao, Y. Liang, H. Liang, Z. Cheng, L. Qu, High rate production of clean water based on the combined photo-electro-thermal effect of graphene architecture, Adv. Mater. (2018), https://doi.org/10.1002/adma.201706805.

[29] P.D. Dongare, A. Alabastri, S. Pedersen, K.R. Zodrow, N.J. Hogan, O. Neumann, J. Wud, T. Wang, A. Deshmukh, M. Elimelech, Q. Li, P. Nordlander, N.J. Halas, Nanophotonics-enabled solar membrane distillation for off-grid water purification, Proc. Natl. Acad. Sci. U. S. A (2017), https://doi.org/10.1073/pnas.1701835114.

[30] L. Huang, J. Pei, H. Jiang, X. Hu, Water desalination under one sun using graphene-based material modified PTFE membrane, Desalination (2018), https://doi.org/10.1016/j.desal.2018.05.006.

[31] X. Han, W. Wang, K. Zuo, L. Chen, L. Yuan, J. Liang, Q. Li, P.M. Ajayan, Y. Zhao, J. Lou, Bio-derived ultrathin membrane for solar driven water purification, Nanomater. Energy (2019), https://doi.org/10.1016/j.nanoen.2019.03.089.

[32] B. Gong, H. Yang, S. Wu, G. Xiong, J. Yan, K. Cen, Z. Bo, K. Ostrikov, Graphene array-based anti-fouling solar vapour gap membrane distillation with high energy efficiency, Nano-Micro Lett. (2019), https://doi.org/10.1007/s40820-019-0281-1.

[33] S. Cao, X. Wu, Y. Zhu, R. Gupta, A. Tan, Z. Wang, Y.S. Jun, S. Singamaneni, Polydopamine/hydroxyapatite nanowire-based bilayered membrane for photothermal-driven membrane distillation, J. Mater. Chem. (2020), https://doi.org/10.1039/c9ta12703h.

[34] I.A. Said, S. Wang, Q. Li, Field demonstration of a nanophotonics-enabled solar membrane distillation reactor for desalination, Ind. Eng. Chem. Res. (2019), https://doi.org/10.1021/acs.iecr.9b03246.

[35] L. Song, Q. Huang, Y. Huang, R. Bi, C. Xiao, An electro-thermal braid-reinforced PVDF hollow fiber membrane for vacuum membrane distillation, J. Membr. Sci. 591 (2019) 117359, https://doi.org/10.1016/j.memsci.2019.117359.

[36] A.V. Dudchenko, C. Chen, A. Cardenas, J. Rolf, D. Jassby, Frequency-dependent stability of CNT Joule heaters in ionizable media and desalination processes, Nat. Nanotechnol. 12 (2017) 557–563, https://doi.org/10.1038/nnano.2017.102.

[37] O.R. Lokare, S. Tavakkoli, V. Khanna, R.D. Vidic, Importance of feed recirculation for the overall energy consumption in membrane distillation systems, Desalination (2018), https://doi.org/10.1016/j.desal.2017.11.037.

[38] E. Deniz, S. Çınar, Energy, exergy, economic and environmental (4E) analysis of a solar desalination system with humidification-dehumidification, Energy Convers. Manag. (2016), https://doi.org/10.1016/j.enconman.2016.07.064.

[39] R. Miladi, N. Frikha, A. Kheiri, S. Gabsi, Energetic performance analysis of seawater desalination with a solar membrane distillation, Energy Convers. Manag. 185 (2019) 143–154, https://doi.org/10.1016/j.enconman.2019.02.011.

[40] M.I. Soomro, W.S. Kim, Performance and economic investigations of solar power tower plant integrated with direct contact membrane distillation system, Energy Convers. Manag. (2018), https://doi.org/10.1016/j.enconman.2018.08.056.

[41] A. Luo, N. Lior, Critical review of membrane distillation performance criteria, Desalin. Water Treat. 57 (2016), https://doi.org/10.1080/19443994.2016.1152637, 20093–20140.

[42] W.L. McCabe, J.C. Smith, P. Harriott, Unit Operations of Chemical Engineering, fourth ed., McGraw-Hill, New York, 1985.

[43] L. Kumar, M. Hasanuzzaman, N.A. Rahim, Global advancement of solar thermal energy technologies for industrial process heat and its future prospects: a review, Energy Convers. Manag. (2019), https://doi.org/10.1016/j.enconman.2019.05.081.

[44] A.A. Hachicha, B.A.A. Yousef, Z. Said, I. Rodríguez, A review study on the modeling of high-temperature solar thermal collector systems, Renew. Sustain. Energy Rev. (2019), https://doi.org/10.1016/j.rser.2019.05.056.

[45] M. Gryta, Effectiveness of Water Desalination by Membrane Distillation Process, Membranes (2012), https://doi.org/10.3390/membranes2030415.

[46] S.O. Olatunji, L.M. Camacho, Heat and mass transport in modeling membrane distillation configurations: a review, Front. Energy Res. 6 (2018) 1–18, https://doi.org/10.3389/fenrg.2018.00130.

[47] F. Banat, N. Jwaied, M. Rommel, J. Koschikowski, M. Wieghaus, Desalination by a "compact SMADES" autonomous solarpowered membrane distillation unit, Desalination 217 (2007) 29–37, https://doi.org/10.1016/j.desal.2006.11.028.

[48] H.E.S. Fath, S.M. Elsherbiny, A.A. Hassan, M. Rommel, M. Wieghaus, J. Koschikowski, M. Vatansever, PV and thermally driven small-scale, stand-alone solar desalination systems with very low maintenance needs, Desalination 225 (2008) 58–69, https://doi.org/10.1016/j.desal.2006.11.029.

[49] A. Criscuoli, M.C. Carnevale, E. Drioli, Evaluation of energy requirements in membrane distillation, Chem. Eng. Process. Process Intensif. 47 (2008) 1098–1105, https://doi.org/10.1016/j.cep.2007.03.006.

[50] X. Wang, L. Zhang, H. Yang, H. Chen, Feasibility research of potable water production via solar-heated hollow fiber membrane distillation system, Desalination 247 (2009) 403–411, https://doi.org/10.1016/j.desal.2008.10.008.

[51] A. Ruiz-Aguirre, J.A. Andrés-Mañas, J.M. Fernández-Sevilla, G. Zaragoza, Experimental characterization and optimization of multi-channel spiral wound air gap membrane distillation modules for seawater desalination, Separ. Purif. Technol. (2018), https://doi.org/10.1016/j.seppur.2018.05.044.

[52] G. Zaragoza, A. Ruiz-Aguirre, E. Guillén-Burrieza, Efficiency in the use of solar thermal energy of small membrane desalination systems for decentralized water production, Appl. Energy (2014), https://doi.org/10.1016/j.apenergy.2014.02.024.
[53] H.C. Duong, A.R. Chivas, B. Nelemans, M. Duke, S. Gray, T.Y. Cath, L.D. Nghiem, Treatment of RO brine from CSG produced water by spiral-wound air gap membrane distillation - a pilot study, Desalination (2015), https://doi.org/10.1016/j.desal.2014.10.026.
[54] R. Schwantes, A. Cipollina, F. Gross, J. Koschikowski, D. Pfeifle, M. Rolletschek, V. Subiela, Membrane Distillation: Solar and Waste Heat Driven Demonstration Plants for Desalination, Desalination (2013), https://doi.org/10.1016/j.desal.2013.04.011.
[55] A. Ruiz-Aguirre, J.A. Andrés-Mañas, J.M. Fernández-Sevilla, G. Zaragoza, Modeling and Optimization of a Commercial Permeate Gap Spiral Wound Membrane Distillation Module for Seawater Desalination, Desalination (2017), https://doi.org/10.1016/j.desal.2017.06.019.
[56] J.A. Andrés-Mañas, A. Ruiz-Aguirre, F.G. Acién, G. Zaragoza, Performance increase of membrane distillation pilot scale modules operating in vacuum-enhanced air-gap configuration, Desalination (2020), https://doi.org/10.1016/j.desal.2019.114202.
[57] R.G. Raluy, R. Schwantes, V.J. Subiela, B. Peñate, G. Melián, J.R. Betancort, Operational Experience of a Solar Membrane Distillation Demonstration Plant in Pozo Izquierdo-Gran Canaria Island (Spain), Desalination (2012), https://doi.org/10.1016/j.desal.2012.01.003.
[58] M. Li, K.J. Lu, L. Wang, X. Zhang, T.S. Chung, Janus membranes with asymmetric wettability via a layer-by-layer coating strategy for robust membrane distillation, J. Membr. Sci. (2020), https://doi.org/10.1016/j.memsci.2020.118031.
[59] E. Guillén-Burrieza, J. Blanco, G. Zaragoza, D.C. Alarcón, P. Palenzuela, M. Ibarra, W. Gernjak, Experimental analysis of an air gap membrane distillation solar desalination pilot system, J. Membr. Sci. 379 (2011) 386–396, https://doi.org/10.1016/j.memsci.2011.06.009.
[60] R. Sarbatly, C.K. Chiam, Evaluation of geothermal energy in desalination by vacuum membrane distillation, Appl. Energy 112 (2013) 737–746, https://doi.org/10.1016/j.apenergy.2012.12.028.
[61] C. Cabassud, D. Wirth, Membrane distillation for water desalination: how to chose an appropriate membrane? Desalination 157 (2003) 307–314, https://doi.org/10.1016/S0011-9164(03)00410-7.
[62] W.G. Shim, K. He, S. Gray, I.S. Moon, Solar energy assisted direct contact membrane distillation (DCMD) process for seawater desalination, Separ. Purif. Technol. 143 (2015) 94–104, https://doi.org/10.1016/j.seppur.2015.01.028.
[63] Q. Ma, A. Ahmadi, C. Cabassud, Direct integration of a vacuum membrane distillation module within a solar collector for small-scale units adapted to seawater desalination in remote places: design, modeling & evaluation of a flat-plate equipment, J. Membr. Sci. 564 (2018) 617–633, https://doi.org/10.1016/j.memsci.2018.07.067.
[64] K. Okiel, A.H.M. El-Aassar, T. Temraz, S. El-Etriby, H.A. Shawky, Vacuum enhanced direct contact membrane distillation for oil field produced water desalination: specific energy consumption and energy efficiency, Desalin. Water Treat. 57 (2016) 11945–11955, https://doi.org/10.1080/19443994.2015.1048305.
[65] E.K. Summers, H.A. Arafat, J.H. Lienhard V, Energy efficiency comparison of single-stage membrane distillation (MD) desalination cycles in different configurations, Desalination 290 (2012) 54–66, https://doi.org/10.1016/j.desal.2012.01.004.
[66] R.K. Shah, A.L. London, Laminar Flow Forced Convection in Ducts: A Source Book for Compact Heat Exchanger Analytical Data, 1978, https://doi.org/10.1016/B978-0-12-020051-1.50022-X.
[67] R.W. Schofield, A.G. Fane, C.J.D. Fell, Heat and mass transfer in membrane distillation, J. Membr. Sci. 33 (1987) 299–313, https://doi.org/10.1016/S0376-7388(00)80287-2.
[68] L.G. Leal, Advanced Transport Phenomena: Fluid Mechanics and Convective Transport Processes, 2007, https://doi.org/10.1017/CBO9780511800245.
[69] J.H. Ferziger, M. Peric, A. Leonard, Computational methods for fluid dynamics, Phys. Today (1997), https://doi.org/10.1063/1.881751.
[70] J. Lou, J. Vanneste, S.C. DeCaluwe, T.Y. Cath, N. Tilton, Computational fluid dynamics simulations of polarization phenomena in direct contact membrane distillation, J. Membr. Sci. (2019), https://doi.org/10.1016/j.memsci.2019.05.074.
[71] M. Dudley, 3-D Numerical Simulations of Conjugate Heat Transport in Vacuum Membrane Distillation Systems with Applied Membrane Heating, Colorado School of Mines, 2020.
[72] J. Vanneste, J.A. Bush, K.L. Hickenbottom, C.A. Marks, D. Jassby, C.S. Turchi, T. Y. Cath, Novel thermal efficiency-based model for determination of thermal conductivity of membrane distillation membranes, J. Membr. Sci. (2018), https://doi.org/10.1016/j.memsci.2017.11.028.